2015 WJTA-IMCA Conference and Expo
November 2-4 ● New Orleans, Louisiana

Paper

NUMERICAL STUDY OF THE CAVITATING JET AND ITS EROSIVITY

Jin-Keun Choi, Chao-Tsung Hsiao, and Georges L. Chahine
DYNAFLOW, INC.
Jessup, Maryland, USA

ABSTRACT

Cavitation enhances waterjets effectiveness for cutting, cleaning, and drilling applications. Understanding the mechanisms involved with the increased erosivity is crucial for improving and controlling jet performance. Here, the cavitating jet flow field is investigated numerically solving the Navier-Stokes equations coupled with bubble dynamics. The jet shear layer forms large structures, which trap the bubble nuclei and enable them to grow explosively. Near the target bubble deformation and reentrant jet formation are found to be very important in generating concentrated shear and high impulsive loads on material layers to be removed.

1 INTRODUCTION

Cavitation enhances the erosivity of submerged waterjets and the efficiency or the removal rate for cutting, cleaning, and drilling applications (Johnson Jr et al.; G L Chahine, Conn, et al.; G L Chahine, Conn, et al.; G L Chahine, Choi, et al.). Cavitating jets are also used for material erosion testing, surface treatment, peening, etc. (Singh, Choi, and Chahine; March; G L Chahine, Choi, et al.; Choi, Jayaprakash, and Chahine; Odhiambo), and understanding the mechanisms involved with the increased erosivity is crucial for designing and improving jet performance.

Microbubble nuclei present in water grow as the water exits the nozzle orifice into the host liquid of lower pressure. The expanded bubbles then collapse energetically on the target surface producing microjets and inducing high impulsive pressures, which result in cleaning or erosion. In order to understand the mechanisms at play, we have investigated the cavitating jet flow field numerically coupling Navier-Stokes and bubble dynamics solutions.

It has been known for more than a century (Besant; Lord Rayleigh) that volume implosion of a bubble can generate very high pressure and shock waves. Many studies have also shown, experimentally as well as analytically, that the collapse of these bubbles near rigid boundaries results in high-speed reentrant liquid jets, which penetrate the highly deformed bubbles to strike a nearby rigid boundary generating water hammer like impact pressures (Knapp, Daily, and Hammitt; Hammitt). The resulting reentrant jet has been found a key element in pit formation on the material surface (C.-T. Hsiao et al.; G. L. Chahine; C-T. Hsiao and Chahine).

Bubble collapse near boundaries has been extensively investigated numerically by assuming flow incompressibility and using the boundary element method (BEM) (Blake; Jayaprakash, Chahine, and Hsiao; Zhang, Duncan, and Chahine; Plesset and Chapman; Chahine, Duraiswami, and Kalumuck). The BEM enables accurate description of the reentrant jet and provides the jet geometric and dynamic characteristics as functions of time and space since the liquid velocities (including the reentrant jet) are small relative to the speed of sound in water. On the other hand, during the bubble explosive growth, rebound, and at jet impact, compressible effects need to be included (A. B. Wardlaw and Luton; A. Wardlaw and Luton). For accurate simulations, we use here a hybrid numerical procedure involving time domain decomposition into incompressible and compressible stages in order to capture the full bubble dynamics including the shock phase occurring during reentrant jet impact, bubble collapse, and bubble rebound.

2 NUMERICAL APPROACH

In order to account for viscous effects in the submerged jet simulations we consider the flow field as a two-phase continuum with a gas volume fraction, α. The density, ρ_m, and kinematic viscosity, μ_m, are related to properties of the gas, ρ_g and μ_g, and those of the liquid, ρ_l and μ_l, through:

$$\rho_{\mathrm{m}} = (1-\alpha)\rho_{\mathrm{l}} + \alpha\rho_{\mathrm{g}}, \qquad \mu_{\mathrm{m}} = (1-\alpha)\mu_{\mathrm{l}} + \alpha\mu_{\mathrm{g}}. \tag{1}$$

The continuity and momentum conservation equations for the mixture are as follows:

$$\frac{\partial \rho_m}{\partial t} + \nabla\left(\rho_m \mathbf{u}_m\right) = 0, \qquad \frac{\partial \rho_m \mathbf{u}_m}{\partial t} + \nabla \rho_m \mathbf{u}_m \mathbf{u}_m = -\nabla p + \nabla \boldsymbol{\tau}, \tag{2}$$

where t is time, $\boldsymbol{u}_m$ the velocity, p the pressure, and $\boldsymbol{\tau}$ the stress tensor. These equations are solved using 3DYNAFS-VIS© (Hsiao, Jain, and Chahine; C.-T. Hsiao et al.; Raju et al.) and a finite volume formulation. 3DYNAFS-VIS has been extensively validated and used to study a range of two-phase problems and its results have compared favorably with available experimental data (G L Chahine).

2.1 Modeling of Bubble Dynamics and Motion

The bubbles are tracked individually and are treated as point sources and dipoles to represent the time variations of their volumes and translation speeds. Volume variations are obtained with a bubble dynamics equation using bubble surface averaged pressures and velocities, to account for flow non-uniformities, and an additional pressure term to account for bubble motion relative to the liquid (G. L. Chahine; Hsiao, Chahine, and Liu). The equivalent bubble radius, R(t), is obtained using a modified Rayleigh-Keller-Herring equation (Prosperetti and Lezzi), which accounts for the compressibility of the surrounding bubbly medium and for flow field non-uniformities:

$$\left(1-\frac{\dot{R}}{c_m}\right)R\ddot{R} + \frac{3}{2}\left(1-\frac{\dot{R}}{3c_m}\right)\dot{R}^2 = \frac{\left(\mathbf{u}_{enc}-\mathbf{u}_b\right)^2}{4} + \frac{1}{\rho_m}\left(1+\frac{\dot{R}}{c_m}+\frac{R}{c_m}\frac{d}{dt}\right)\left[p_v + p_{g_0}\left(\frac{R_0}{R}\right)^{3k} - p_{enc} - \frac{2\sigma}{R} - 4\mu_m\frac{\dot{R}}{R}\right], \tag{3}$$

where c_m is the local sound speed in the two-phase medium and $\mathbf{u}_b$ is the bubble translation velocity. p_{enc} and $\mathbf{u}_{enc}$, the "encountered" pressure and velocity respectively, are the pressures and velocities in the two-phase medium averaged over the bubble surface. The introduction of $\mathbf{u}_{enc}$ and p_{enc} in Equation (3) is to account for non-uniform pressures and velocities around the bubble and for slip velocity between the bubble and the host medium. Using these average values instead of the conventionally used values at the bubble center, results in a major improvement over classical models (G. L. Chahine; Hsiao, Chahine, and Liu).

The bubble trajectory is obtained using the following motion equation

$$\frac{d\mathbf{u}_b}{dt} = -\frac{3}{\rho_m}\nabla p - 2g + \frac{3}{4}\frac{C_D}{R}\left(\mathbf{u}_{enc}-\mathbf{u}_b\right)\left|\mathbf{u}_{enc}-\mathbf{u}_b\right| + \frac{3}{2\pi}\frac{C_L}{R}\sqrt{\frac{\mu_m}{\rho_m}}\frac{\left(\mathbf{u}_{enc}-\mathbf{u}_b\right)\times\boldsymbol{\omega}}{\sqrt{|\boldsymbol{\omega}|}} + \frac{3}{R}\left(\mathbf{u}_{enc}-\mathbf{u}_b\right)\dot{R},$$
$$C_D = \frac{24}{R_{eb}}\left(1+0.197R_{eb}^{0.63}+2.6\times10^{-4}R_{eb}^{1.38}\right), \qquad R_{eb} = \frac{2\rho_m R\left|\mathbf{u}_{enc}-\mathbf{u}_b\right|}{\mu_m}. \tag{4}$$

where $\boldsymbol{\omega}$ is the local vorticity, g is the acceleration of gravity, C_L is the lift coefficient, and C_D is the drag coefficient given by (Haberman and Morton). The added mass term is indirectly represented by the first term of the right hand side where $d\mathbf{u}_{enc}/dt$ has been replaced by the

$\nabla p / \rho_m$ term. The last term is a force due to coupling between bubble volume oscillations and bubble motion (Johnson and Hsieh).

2.2 Bubble-Flow Motion Coupling

The two-way coupling between the medium and the bubbles has as key the deduction of the void fraction distribution from the instantaneous bubble sizes and locations. This is realized as follows:

- The volume change and the motion of the individual bubbles in the flow field are controlled by the two-phase medium local properties and flow field gradients.
- The local properties of the mixture (void fractions and local densities) are determined by the spatial distribution of the bubble and by their volumes.
- The mixture flow field with evolving mixture density distribution satisfies mass and momentum conservation.

2.3 Bubble Collapse Modeling

Our numerical approach to model bubble collapse and material response uses a hybrid approach able to simulate fluid structure interaction (FSI) problems involving shock and bubble pressure pulses (C.-T. Hsiao and Chahine; Chahine, Raju, and Hsiao). During growth of a cavitation bubble an incompressible Boundary Element Method (BEM) code 3DYNAFS-BEM© (Chahine & Perdue 1989, Chahine & Kalumuck 1998, Choi & Chahine 2003) is used to simulate most of the bubble period until the end of the bubble collapse where, due to high liquid speeds or to the bubble reentrant jet impacting on the liquid or on the structure, compressible flow effects prevail again. The BEM method has been shown to provide reentrant jet parameters and speed accurately (Chahine and Perdue; Zhang, Duncan, and Chahine; J.-K. Choi and Chahine; Jayaprakash, Singh, and Chahine). The solution of the BEM code is then passed to a fully compressible code capable of shock capturing to simulate reentrant jet impact and bubble ring collapse. The compressible flow solver 3DYNAFS-COMP© (Kapahi, Hsiao, and Chahine) is used and enables modeling shock propagation, liquid-liquid, and liquid-solid impacts.

3 NUMERICAL RESUTS

3.1 Cavitating Jet Flow Field

A nozzle with hemispherical contraction upstream of the orifice is considered. The nozzle has an orifice with diameter, dj = 0.064", and the length of the orifice is 0.064". We considered a flow of 5.5 gpm at a pressure drop of 4,200 psi across the orifice. Figure 1 shows the computational mesh to model this nozzle and the flow field between the nozzle and a target wall to be cleaned or eroded.

As shown in Figure 2, the jet exiting the nozzle has a hat velocity profile with the maximum speed on the axis. Viscous friction with the surrounding liquid diffuses the jet, widens it, and generates vortices, which become structured and modify significantly the flow. The jet speed is

seen in Figure 2 to form regular organized structures close to the nozzle, while the jet speed on the jet edge decay significantly. Similarly, the jet speed decays as the liquid moves away from the nozzle.

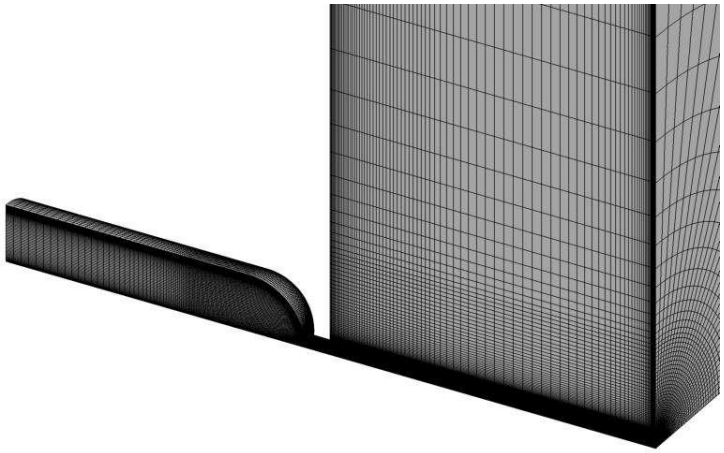

Figure 1. Computational mesh for the jet flow modeling.

The thickness of the boundary layer at the wall depends on the local liquid speed. This has strong implications on cleaning as microscopic particles at the wall are often embedded in the very low speed boundary layer and the shear exerted on them is unable to dislodge them. This strong vortex generation can then be purposely sought and enhanced through jet nozzle design for strong acoustic resonance (G L Chahine, Conn, et al.; Kalumuck et al.). At the wall, as the incoming jet velocity fluctuates, the shear flow has also to adapt and as seen in Figure 3, and ends up exhibiting a very intensely varying shear flow configuration in both time and space.

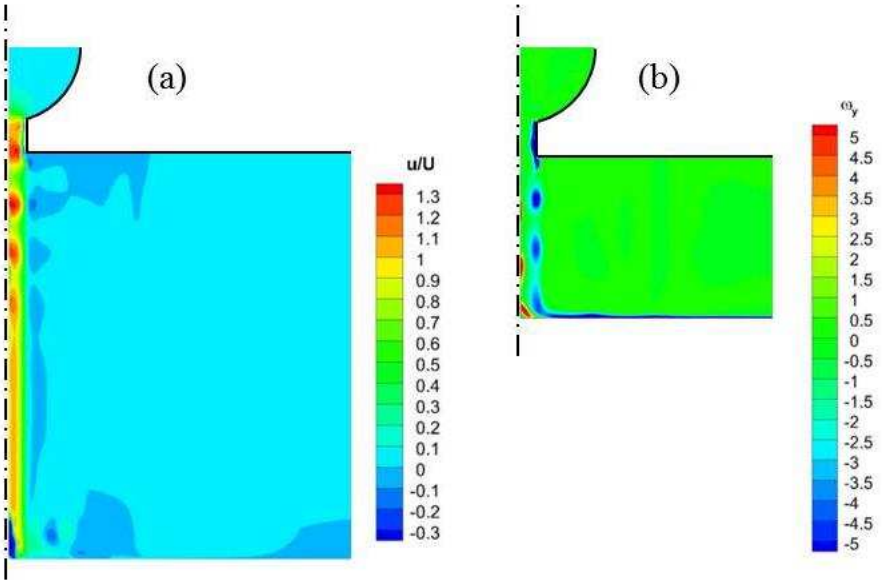

Figure 2. (a) Contours of non-cavitating axial velocity normalized by the mean jet velocity. Wall distance = 13 orifice diameters. (b) Vorticity contours when the wall is distance is 5 orifice diameters.

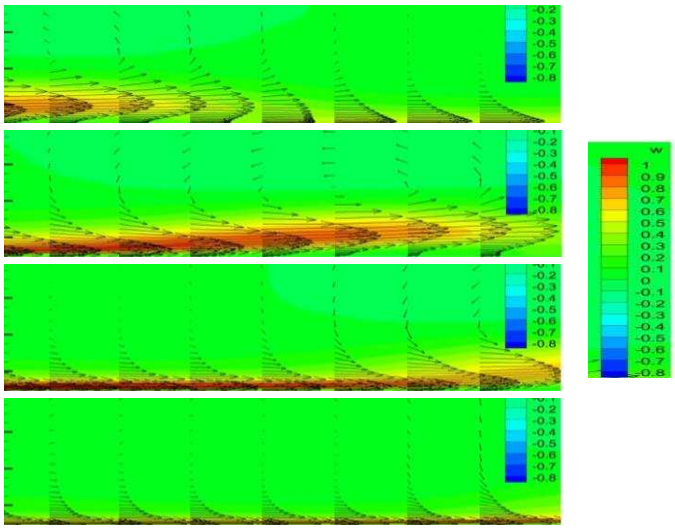

Figure 3. Time sequence of radial velocity contours near the wall at a distance from the jet axis of two jet diameters. Time between images is 1.44 μs. Wall at 13 orifice diameters from the orifice.

In order to account for bubble dynamics, bubble nuclei are randomly dispersed in the liquid and tracked in the simulations. These microscopic or nanoscopic nuclei are omnipresent in any liquids (G L Chahine; Mørch) unless extreme precautions are taken to produce ultra-pure liquids, in which case there still is a chance to have undetected nanoscopic bubble nuclei. As described earlier, a Lagrangian procedure is used to track these nuclei and determine their position and volume in space and time. This is fed back to the mixture flow and provides the void fraction at each location necessary to advance the solution. Knowledge of the bubble dynamics and the fluid dynamics then enables one to determine fluctuating shear and pressures at the cleaned surface.

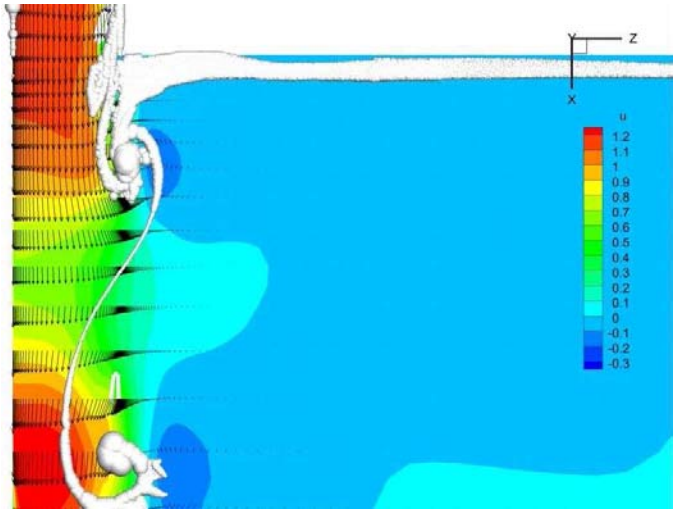

Figure 4. Flow field of a cavitating jet showing bubble capture and growth of ring and longitudinal vortices. White contours are larger cavities represented by a level set scheme.

In this study, two nuclei sources are considered. The first is surface nucleation where nuclei from the rigid surfaces are emitted when the pressure decreases below the vapor pressure. The second source is free field nuclei: here for illustration 20 μm bubbles with a void fraction of about 1%.

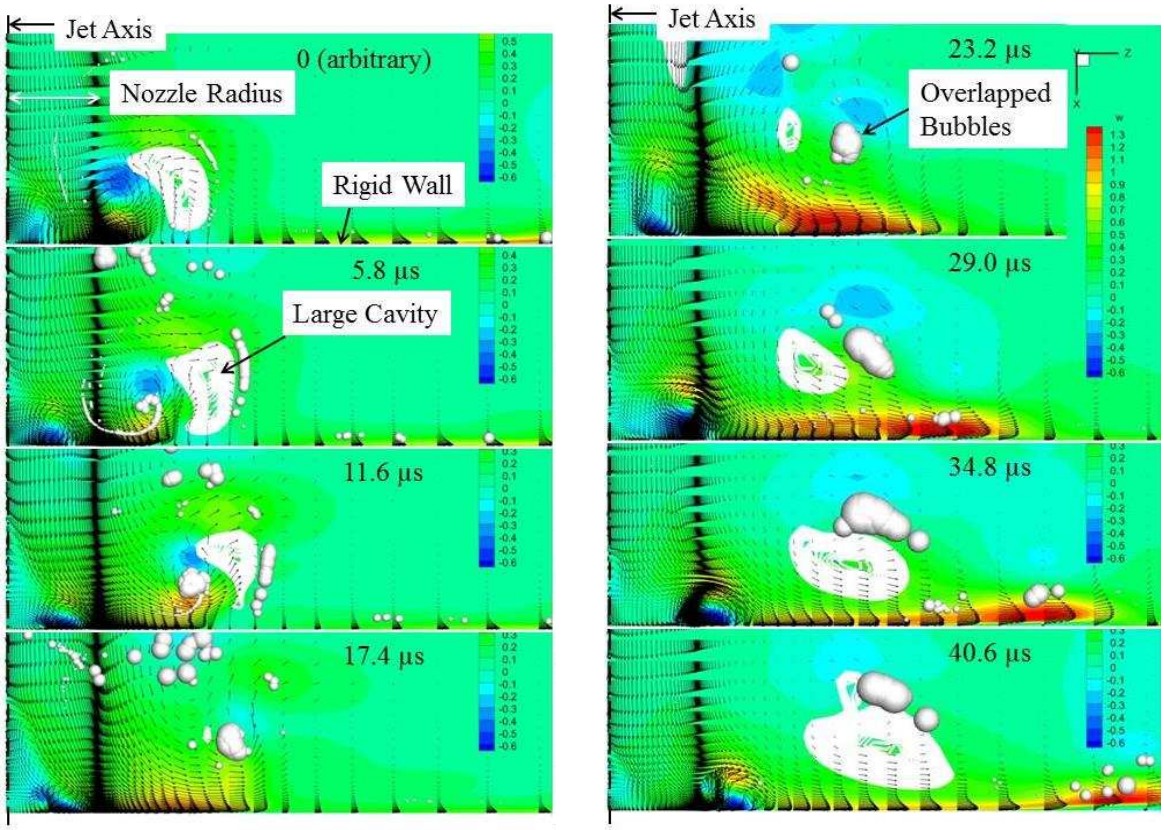

Figure 5. Velocity vectors, cavitation bubbles, and contours of radial velocity (parallel to the wall) for a cavitating jet impinging on a wall. The time sequence is left top to bottom, then right top to bottom. Time between images is 5.8 µs. Wall at 13 jet diameters from the orifice. The radial velocities are normalized by the mean jet velocity.

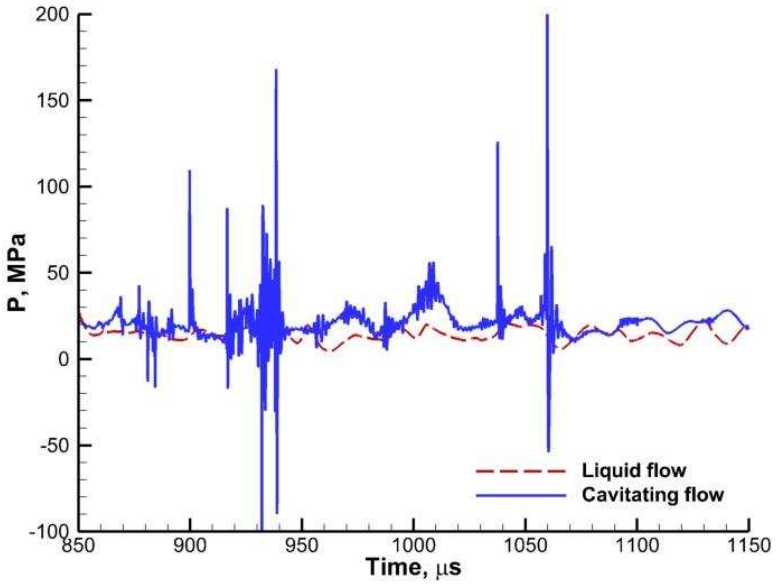

Figure 6. Time history of pressure at wall at the jet impingement center. The red curve is obtained for the jet flow in absence of nuclei seeding, while the green curve includes nuclei seeding and cavitation.

Figure 4 shows an illustrative example for the two-way coupled (bubble-liquid and liquid-bubble) simulations of a cavitating jet. The flow field near the nozzle orifice is nicely illustrated by the velocity vectors and their evolution as the distance from the nozzle increases. A more impressive illustration of the flow field is seen through the nuclei captured from the face of the nozzle into the shear layer. These nuclei grow and are captured by the large vortical structure at the edge of the submerged jet. These structures form two modes: an azimuthal mode resulting in vortex rings and a longitudinal mode that results in elongated vortices which join two vortical ring structures. This is very well visualized by the bubbles captured in the vortices and clearly seen in the figure. Later on as the jet advances to hit the wall (Figure 5), the bubbles grow into larger clouds, which collapse at or near the wall. The passage of the structures and the bubbles further induces fluctuations in the wall pressures and shear. A very large difference in the generated pressure field between cavitating and non-cavitating jet is clearly seen in Figure 6. Cavitation induces orders of magnitude larger pressures relative to the non-cavitating jet (red curve) in both number and amplitude of impulsive pressures due to the collapsing bubbles (green curve).

The vortices generated in the shear layer of the jet forms vortex rings first, and then the vortex rings tends to break into longitudinal vortices. In Figure 7 left, iso-vorticity surfaces are shown where the longitudinal component develops as the jet flows away from the orifice. Small bubble nuclei tend to grow when they are entrained by the vortices. Figure 7 right shows an overview of the cavitating jet. Numerous bubbles flow with the jet, some of them grow as they are entrained into the vortex structures of the jet. Due to the low pressure in the vortex core, the cavitation bubbles grow and then collapse at the wall.

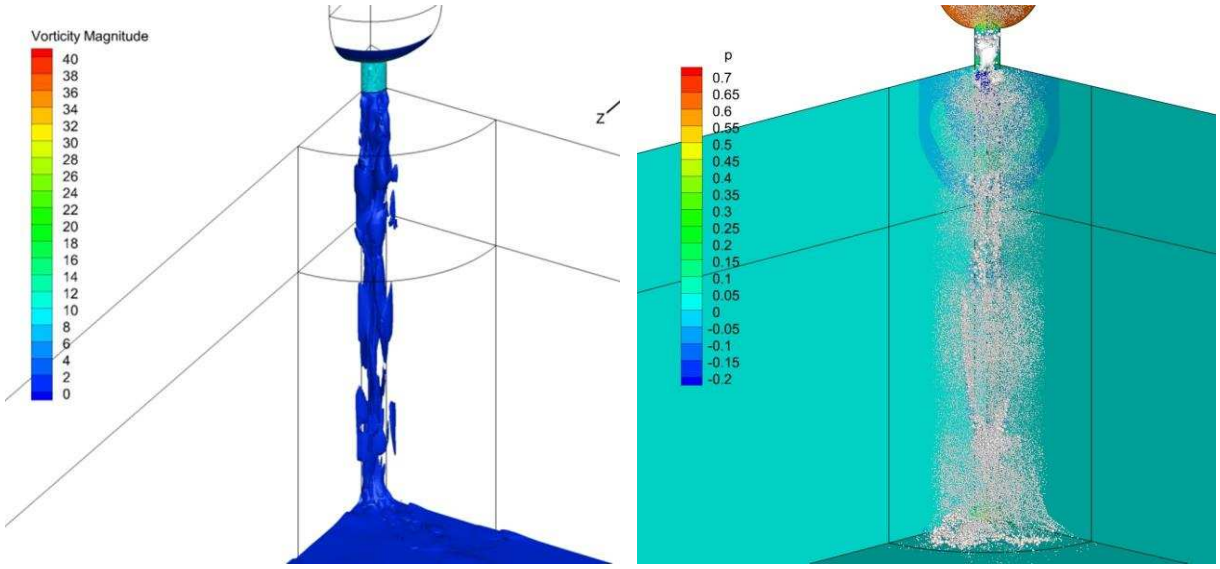

Figure 7. Vorticity contours and iso-vorticity surface sowing the dimensionless vorticity, $|\omega| = 2$ (left), and cavitation bubbles which tend to concentrate along the vortex structures in the jet (right).

3.2 Cavitation Bubble Collapse near Wall

In this section, we examine the pressure loading generate by a collapsing bubble. This requires studying the dynamics of single bubbles near the wall. We consider an initially spherical bubble of radius 50 μm, located at a distance of $X = 1.5\text{mm}$ from a flat material surface and subject it to a time-varying pressure field as represented in Figure 8 and expressed as follows:

$$p(t) = \begin{cases} 10^5\,\text{Pa}; & t < 0, \\ 10^3\,\text{Pa}; & 0 \le t \le 2.415\text{ms}, \\ 10^7\,\text{Pa}; & t > 2.415\text{ms}. \end{cases} \tag{5}$$

Figure 8b shows the time history of the bubble radius in response to the imposed pressure field obtained by solving the Rayleigh-Plesset equation ignoring for now the presence of the wall. It is seen that the bubble starts an explosive grow as soon as the pressure suddenly drops to a low pressure below the critical pressure. The bubble continues to grow until the pressure rises again to a high value. This time-varying pressure field is set up to mimic the encountered pressure for a traveling cavitation bubble in a cavitating jet and arriving at the stagnation region near the wall.

To simulate the bubble dynamics near the wall, the incompressible BEM solver is first applied with a total of 400 nodes and 800 panels used to discretize the bubble surface. This corresponds to a grid density, which provides grid independent solution (Chahine, Duraiswami, and Kalumuck). Figure 9 shows the variations of the bubble outer contours as time advances. As the bubble grows between $t = 0$ and $t \sim 2.4$ms, it behaves almost spherically on its portion away from the wall, while the side close to the material flattens and expands in the direction parallel to the wall actually never touching the wall as a layer of liquid remains between the bubble and the wall. Such a behavior has been confirmed experimentally by (Chahine, Duraiswami, and Kalumuck).

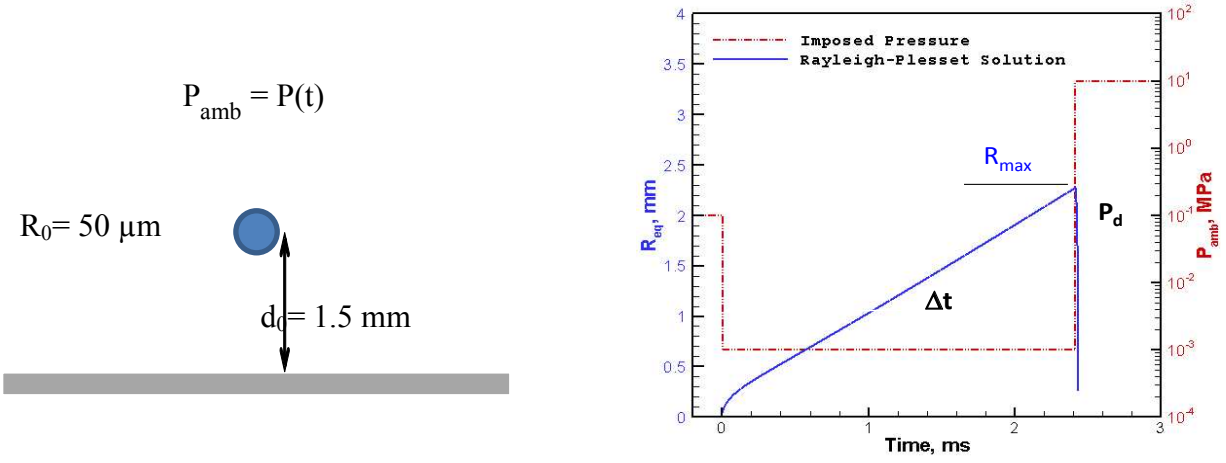

Figure 8. (a) Illustration of the problem of a bubble growth and collapse near a wall. Initial spherical bubble radius 50 μm at 1.5 mm distance from the wall. (b) Imposed time-varying pressure field and resulting time history of the bubble radius obtained by solving the Rayleigh-Plesset equation.

The bubble continues expanding following pressure reversal due to the inertia of the outward flow of the liquid. Due to the asymmetry of the flow, the pressures at the bubble interface on the

side far from the wall are much higher than those near the material; thus the collapse proceeds with the far side moving towards the material wall. The resulting acceleration of the liquid flow perpendicular to the bubble free surface develops into a reentrant jet that penetrates the bubble and moves much faster than the rest of the bubble surface to impact the opposite side of the bubble and the material boundary.

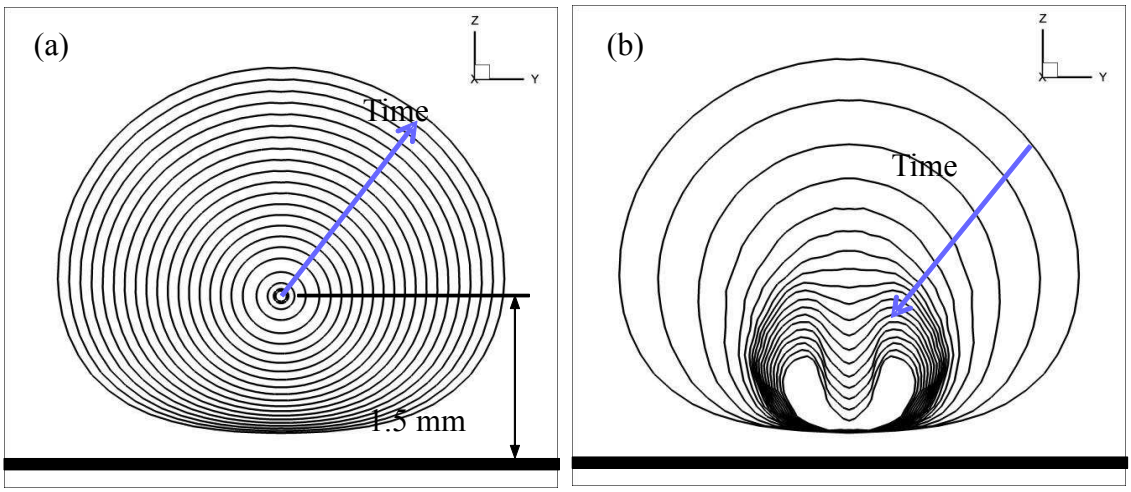

Figure 9. Bubble shape outlines at different times showing (a) bubble growth ($0 < t < 2.415$ ms) and (b) collapse (2.415 ms $< t < 2.435$ms). Results obtained by the 3DYNAFS-BEM© simulations for $R_0 = 50$ μm, $P_d = 10$ MPa, $\bar{X} = 0.75$, and p(t) described by Equation (5).

3.3 Reentrant Jet Impact and Bubble Ring Collapse

The simulation of the bubble dynamics is then switched from the BEM to the compressible flow solver right before the jet touches the opposite side of the bubble (dubbed touchdown). The compressible flow solver is used to continue the simulation. An axisymmetric 1 m × 1 m domain with a total of 220 × 1,470 grid points with stretched grids concentrated in the immediate region surrounding the bubble is used. The grids are distributed such that there is a uniform fine mesh with a size of 10 μm in the area of interest where the interaction between bubble and plate is important as shown in Figure 10. A reflection boundary condition is imposed on the axis of symmetry, i.e. all physical variables such as density, pressure, velocities and energy are reflected from the axis, while transmission non-reflective boundary conditions (i.e. the flow variables are extrapolated along the characteristic wave direction) are imposed at the far field boundaries.

Figure 11 shows the bubble shapes and the corresponding pressure contours computed at six time instances after jet impact. It is seen that after 0.05 μs the jet has completely penetrated the bubble and touched the opposite side. The liquid-liquid impact event generates a localized high pressure region which then expands quasi spherically to reach the material liquid interface after 0.2 μs. The volume of the bubble ring remaining after the jet touchdown shrinks and reaches a minimum at $t - t_{link} = 0.7$ μs. The collapse of the bubble ring generates another high pressure wave, which then propagates toward the axis of the cylindrical domain and reaches the wall at $t - t_{link} = 0.9$ μs.

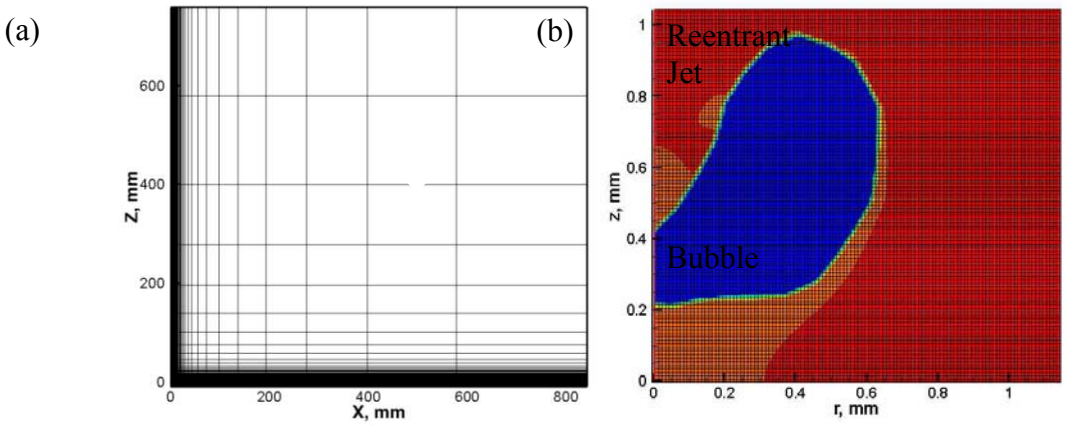

Figure 10. Axisymmetric computational domain used for the computation of the bubble dynamics by the compressible flow solver: (a) full domain, (b) zoom on the bubble/wall region. The blue region is the inside of the bubble after it formed a reentrant jet on the axis of symmetry, which is the Z-axis here.

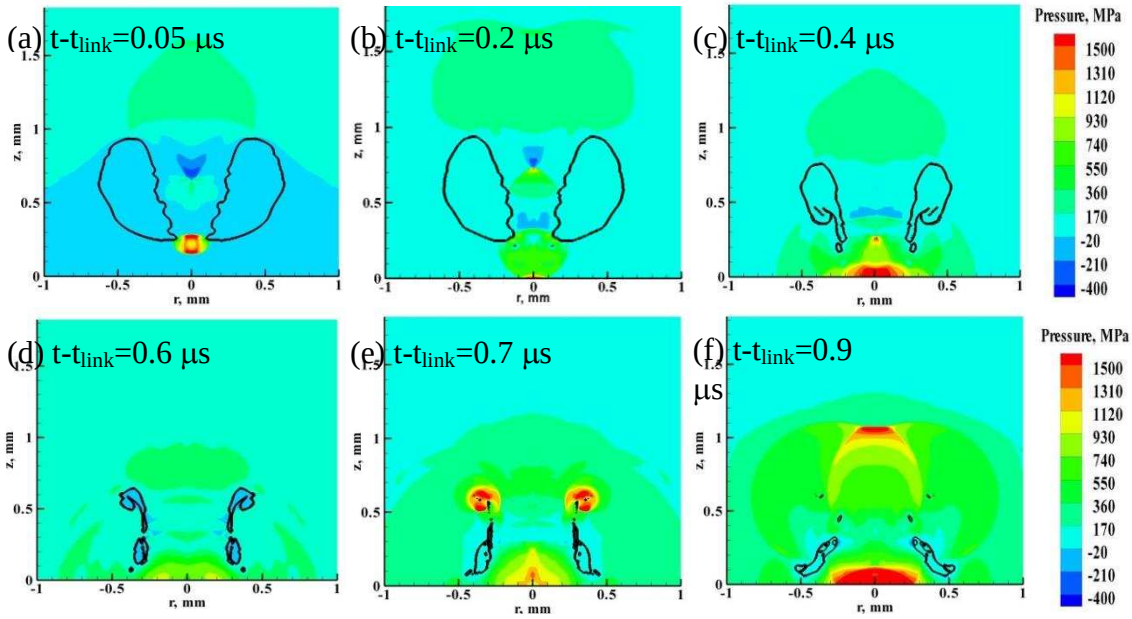

Figure 11. Pressure contours and bubble outlines at different instances following reentrant jet touchdown. Initial bubble radius R_0 = 50 µm, R_{max} = 2 mm, d_0=1.5mm, the initial standoff $\overline{X}$ = 0.75, and collapse driving pressure P_d = 10 MPa.

The pressures generated are seen to exceed 1.5 GPa and explain the strong erosive effect of cavitating jets. Material response for Al7075 was obtained by using an FEM code, fully coupled with the fluid simulation. The time histories of the liquid pressure and the vertical displacement of the material surface at the center of the Al7075 plate / liquid interface are shown together in Figure 12. The material starts to get compressed as the high pressure loading due to the reentrant jet impact reaches it, and the plate surface center point starts to move into the material direction at t - t_{link} = 0.45 µs. The maximum deformation occurs when the highest pressure loading peak due to the bubble ring collapse reaches the center of the plate at time t - t_{link} = 1.15 µs. Once the pressure loading due to the full bubble dynamics has virtually vanished at t - t_{link} = 4 µs, the surface elevation continues to oscillate due to stress waves propagating back and forth through

the metal alloy thickness and lack of damping in the model. Finally, a permanent deformation in the form of a pit remains as a result of the high pressure loading causing local stresses that exceed the Al7075 elastic limit. The vertical displacement of the monitored location eventually converges to a non-zero value of about 9 μm.

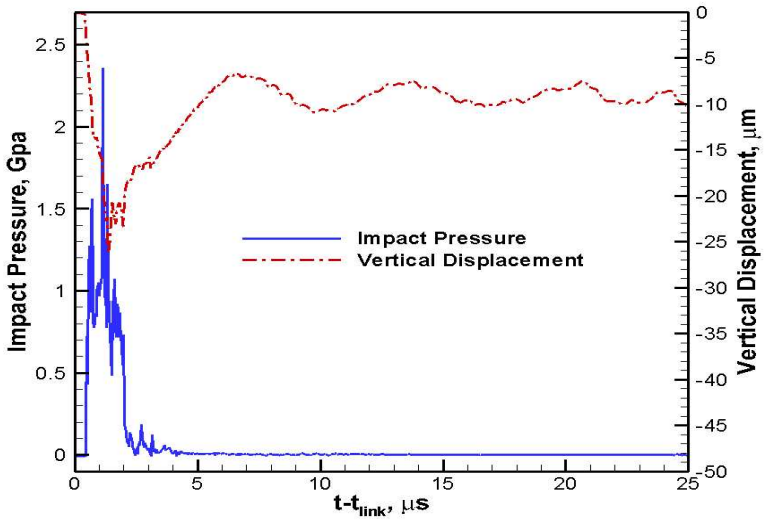

Figure 12. Time history of the pressure and vertical displacement at the top surface center of an Al7075 plate following the collapse of a cavitation bubble. R_0 = 50 μm, R_{max} = 2 mm, P_d = 10 MPa, and $\bar{X} = 0.75$.

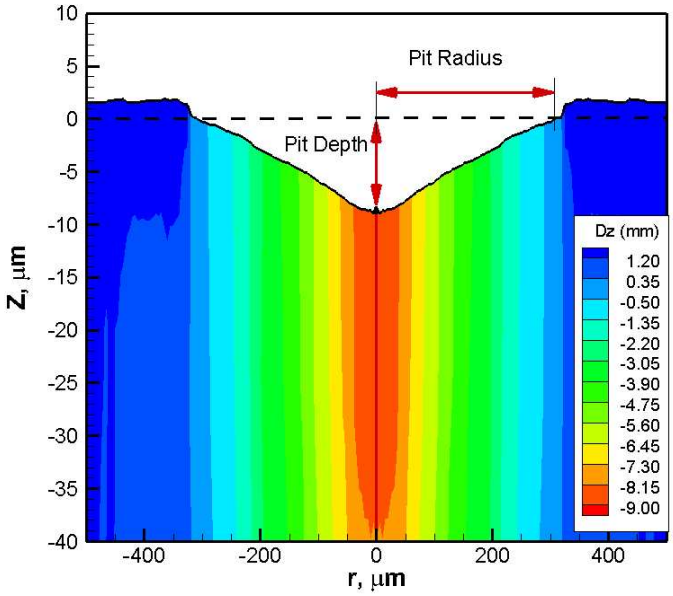

Figure 13. Profile of the permanent deformation of an Al7075 plate following the collapse of a cavitation bubble. R_0 = 50 μm, R_{max} = 2 mm, P_d = 10 MPa, and $\bar{X} = 0.75$.

Finally, the impacted region bears a permanent deformation as shown in Figure 13. The profile of the permanent deformation generated on the plate surface reproduces that of the observed cavitation generated pit shapes (Philipp and Lauterborn; Kim et al.). Further details can be found in (Chahine and Hsiao; Chao-Tsung Hsiao et al.; Choi et al.).

4 CONCLUSIONS

Cavitating jet flow field was modeled using a coupled viscous flow and bubble dynamics approach, which handles the bubbly mixture flow and tracking and volume change of the bubble nuclei in the flow. The two schemes were fully coupled, where the mixture flow fields provides pressure and velocity for bubble simulations, whereas the results of bubble dynamics modifies the void fraction distribution in the mixture flow field. For individual bubbles, a Boundary Element Method was used first to follow the reentrant jet development, and then a compressible flow solver was used during the shock wave propagation and reentrant jet impact on the wall.

The modeled cavitating jet flow shows the tendency of the jet to form large structures, which trap the nuclei and enable them to grow into relatively large bubbles. Bubble deformation and reentrant jet formation are seen to be very important on generating concentrated shear and high impulsive loads on the material surface to be cleaned. The pressure loading on the material surface during the bubble collapse is shown to be due to the reentrant jet impact and to the collapse of the remaining bubble ring.

5 ACKNOWLEDGEMENTS

This work was conducted under support from DYNAFLOW, INC. internal IR&D and partial support from the Office of Naval Research under Contract N00014-12-M-0238, monitored by Dr. Ki-Han Kim. We would like to thank Dr. Kim for his support.

6 REFERENCES

Besant, W. A Treatise on Hydrostatics and Hydrodynamics. Deighton: N.p., 1859. Print.

Blake, J. “Cavitation Bubbles Near Boundaries.” Annual Review of Fluid Mechanics 1987: 99–123. Print.

Chahine, G L, A F Conn, et al. “Cleaning and Cutting with Self-Resonating Pulsed Water Jets.” 2nd U.S. Water Jet Conference. Rolla, Missouri: N.p., 1983. 167–176. Print.

2Chahine, G L, J-K. Choi, et al. “Development of a Diver-Operated Propeller Cleaning System Using the DYNAJETS® Enhanced Cavitation Jets .” Dynaflow, Inc. Technical Report 2M13001-1-ONR (2014): n. pag. Print.

Chahine, G L. “Nuclei Effects on Cavitation Inception and Noise.” 25th Symposium on Naval Hydrodynamics. St. John’s, NL, Canada: N.p., 2004. Print.

---. “Numerical Simulation of Bubble Flow Interactions.” Journal of Hydrodynamics. Vol. 21. Warwick University, UK: N.p., 2008. 316–332. Print.

Chahine, G L, A F Conn, et al. “Passively Interrupted Impulsive Water Jets.” 6th International Conference on Erosion by Liquid and Solid Impact. Cambridge England: N.p., 1983. Print.

Chahine, G L, J-K. Choi, et al. Study of Cavitation Erosion Prediction: Testing, Modeling, and Scaling. N.p., 2009. Print.

Chahine, G L, and K Kalumuck. “BEM Software for Free Surface Flow Simulation Including Fluid Structure Interaction Effects.” International Journal of Computer Applications for Technology 11.3-5 (1998): 177–198. Print.

Chahine, G L, and T O Perdue. “Simulation of the Three-Dimensional Behavior of an Unsteady Large Bubble Near a Structure.” 3rd International Colloquium on Drops and Bubbles. Ed. T G Wang. Monterey, CA: American Institue of Physics, 1988. 188–199. Print.

Chahine, G L, R Raju, and C-T. Hsiao. “Simulation of the Bubble Collapse Near a Wall: HandBack from 3DynaFS (c) to Gemini.” Dynaflow, Inc. Technical Report 2M9007-NSWCIH-1 (2010): n. pag. Print.

Chahine, G. L. “Modeling of Cavitation Dynamics and Interaction with Material.” Advanced Experimental and Numerical Techniques for Cavitation Erosion Prediction. Ed. A. Kim, K-H, Chahine, G.L., Franc, J-P., Karimi. Berlin: Springer, 2014. 123–173. Print.

Chahine, G. L., R. Duraiswami, and K. M. Kalumuck. “Boundary Element Method for Calculating 2-D and 3-D Underwater Explosion Bubble Behavior in Free Water and Near Structures.” Naval Surface Warfare Center, Weapons Research and Technology Department Report NSWCDD/TR-93/46 (1996): n. pag. Print.

Chahine, G. L., and C.-T. Hsiao. “Modeling Cavitation Erosion Using Fluid-Material Interaction Simulations.” Royal Society Meeting Amazing (Cavitation) Bubbles: Great Potentials and Challenges. Buckinghamshire, UK: N.p., 2014. Print.

Choi, J. K., and G. L. Chahine. “Non-Spherical Bubble Behavior in Vortex Flow Fields.” Computational Mechanics. Vol. 32. Austin, TX: N.p., 2003. 281–290. Web.

Choi, J.-K., and G L Chahine. “A Numerical Study on the Bubble Noise and the Tip Vortex Cavitation Inception.” 8th International Conference on Numerical Ship Hydrodynamics. Vol. 7. Busan, Korea: N.p., 2003. 13–33. Print.

Choi, J-K Jin-Keun et al. “Relationship between Space and Time Characteristics of Cavitation Impact Pressures and Resulting Pits in Materials.” Journal of Materials Science 49.8 (2014): 3034–3051. Web.

Choi, J-K., A Jayaprakash, and G L Chahine. “Scaling of Cavitation Erosion Progression with Cavitatin Intensity and Cavitation Source.” Wear 278-279 (2012): 53–61. Print.

Haberman, William L., and Rose K. Morton. “An Experimental Study of Bubbles Moving in Liquids.” Transactions of the American Society of Civil Engineers 121.1 (1956): 227–250. Web. 26 Aug. 2015.

Hammitt, F. G. Cavitation and Multiphases Flow Phenomena. McGraw-Hill, 1980. Print.

Hsiao, C.-T. et al. “Numerical and Experimental Study of Bubble Entrainment Due to a Horizontal Plunging Jet.” International Shipbuilding Progress 60.1 (2013): 435–469. Print.

Hsiao, C.-T., and G. L. Chahine. “Development of Compressible-Incompressible Link to Efficiently Model Bubble Dynamics near Floating Body.” Advances in Boundary Element & Meshless Techniques XIV. Paliseau, France: N.p., 2013. Print.

Hsiao, C.-T., A Jain, and and G L Chahine. “Effect of Gas Diffusion on Bubble Entrainment and Dynamics around a Propeller.” 26th Symposium on Naval Hydrodynamics. Rome, Italy: N.p., 2006. Print.

Hsiao, Chao-Tsung et al. “Modelling of Material Pitting from Cavitation Bubble Collapse.” Journal of Fluid Mechanics 755 (2014): 142–175. Web.

Hsiao, C-T., and G L Chahine. “Dynamic Response of a Composite Propeller Blade Subjected to Shock and Bubble Pressure Loading.” 83rd Shock and Vibration Symposium. New Orleans, LA: N.p., 2012. Print.

Hsiao, C-T., G L Chahine, and H Liu. “Scaling Effects on Prediction of Cavitation Inception in a Line Vortex Flow.” ASME Journal of Fluids Engineering 125.1 (2003): 53–60. Print.

Jayaprakash, A., G. L. Chahine, and C.-T. Hsiao. “Numerical and Experimental Study of the Interaction of a Spark-Generated Bubble and a Vertical Wall.” ASME Journal of Fluids Engineering 134.3 (2012): 31301–31312. Print.

Jayaprakash, A., S. Singh, and G. L. Chahine. “Experimental and Numerical Investigation of Single Bubble Dynamics in a Two-Phase Bubbly Medium.” ASME Journal of Fluids Engineering 133.12 (2011): 121305–121309. Print.
Johnson Jr, V et al. “The Development of Structured Cavitating Jets For Deep-Hole Bits.” 57th Annual Fall Technical Conf & Exhibition of the Society of Petroleum Engineers of ASME. New Orleans, Louisiana: N.p., 1982. Print.
Johnson, V E, and T Hsieh. “The Influence of the Trajectories of Gas Nuclei on Cavitation Inception.” Sixth Symp. Naval Hydrodynamics (1966): 163–179. Web. 24 Feb. 2015.
Kalumuck, K M et al. “Development of a DynaJet Cavitating Water Jet Cleaning Tool for Underwater Marine Fouling Removal.” Proceedings of the 9th American Water Jet Conference. Vol. 2. Dearborn, MI: N.p., 1997. 541–554. Print.
Kapahi, A., C.-T. Hsiao, and G. L. Chahine. “A Multi-Material Flow Solver for High Speed Compressible Flow Applications.” Computers in Fluids (2015): DOI: 10.1016/j.compfluid.2015.03.016. Web.
Kim, K-H. et al. Advanced Experimental and Numerical Techniques for Cavitation Erosion Prediction. Ed. Ki-Han Kim et al. Vol. 106. Springer Netherlands, 2014. Print. Fluid Mechanics and Its Applications.
Knapp, R T, J W Daily, and F G Hammitt. Cavitation. London: McGraw-Hill, 1970. Print.
Lord Rayleigh. “On the Pressure Developed in a Liquid during the Collapse of a Spherical Cavity.” Philosophical Magazine Series 6 34.200 (1917): 94–98. Print.
March, P A. “Evaluating the Relative Resistance of Materials to Cavitation Erosion: A Comparison of Cavitating Jet Results and Vibratory Results.” Cavitation and Multiphase Flow Forum. Cincinnati, OH: American Society of Mechanical Engineers, 1987. Print.
Mørch, K.A. KA. “Cavitation Nuclei: Experiments and Theory. Journal of Hydrodynamics.” Journal of Hydrodynamics, Ser. B 21.2 (2009): 176–189. Print.
Odhiambo, D. “Cavitation Shotless Peening for Improvement of Fatigue Strength of Carbonized Steel.” International Journal of Fatigue 25.9-11 (2003): 1217–1222. Web. 28 July 2015.
Philipp, A., and W. Lauterborn. “Cavitation Erosion by Single Laser-Produced Bubbles.” Journal of Fluid Mechanics 1998: 75–116. Print.
Plesset, Milton S., and Richard B. Chapman. “Collapse of an Initially Spherical Vapour Cavity in the Neighbourhood of a Solid Boundary.” Journal of Fluid Mechanics 1971: 283. Print.
Prosperetti, A., and A. Lezzi. “Bubble Dynamics in a Compressible Liquid. Part 1. First-Order Theory.” Journal of Fluid Mechanics 1986: 457. Print.
Raju, Reni et al. “Study of Pressure Wave Propagation in a Two-Phase Bubbly Mixture.” ASME Journal of Fluids Engineering 133.12 (2011): 121302–121312. Web.
Singh, S., J-K. Choi, and G. L. Chahine. “Characterization of Cavitation Fields From Measured Pressure Signals of Cavitating Jets and Ultrasonic Horns.” Journal of Fluids Engineering 135.9 (2013): 9111–91302. Web.
Wardlaw, A, and J A Luton. “The Gemini Euler Solver for the Coupled Simulation of Underwater Explosions.” NSWCIH - Technicak Report 2500 (2003): n. pag. Print.
Wardlaw, Andrew B, and J Alan Luton. “Fluid-Structure Interaction Mechanisms for Close-in Explosions.” Shock and Vibrations 7 (2000): 265–275. Print.
Zhang, S, J Duncan, and G L Chahine. “The Final Stage of the Collapse of a Cavitation Bubble Near a Rigid Wall.” Journal of Fluid Mechanics 257 (1993): 147–181. Print.